SANDIA REPORT
SAND 2012-7837
Unlimited Release
Printed September 2012

Scalable Assembly of Patterned Ordered Functional Micelle Arrays: Final LDRD Report

Hongyou Fan, Zaicheng Sun, Feng Bai, Anh Ta, Raid E. Haddad, Daniel M. Boye, Kevin A. Arpin, James H. Pikul, William P. King, and Paul V. Braun

Prepared by
Sandia National Laboratories
Albuquerque, New Mexico 87185 and Livermore, California 94550

Sandia National Laboratories is a multi-program laboratory managed and operated by Sandia Corporation,
a wholly owned subsidiary of Lockheed Martin Corporation, for the U.S. Department of Energy's
National Nuclear Security Administration under contract DE-AC04-94AL85000.

Issued by Sandia National Laboratories, operated for the United States Department of Energy by Sandia Corporation.

Available to DOE and DOE contractors from
U.S. Department of Energy
Office of Scientific and Technical Information
P.O. Box 62
Oak Ridge, TN 37831

Telephone: (865) 576-8401
Facsimile: (865) 576-5728
E-Mail: reports@adonis.osti.gov
Online ordering: http://www.osti.gov/bridge

Available to the public from
U.S. Department of Commerce
National Technical Information Service
5285 Port Royal Rd.
Springfield, VA 22161

Telephone: (800) 553-6847
Facsimile: (703) 605-6900
E-Mail: orders@ntis.fedworld.gov
Online order: http://www.ntis.gov/help/ordermethods.asp?loc=7-4-0#online

SANDIA REPORT

SAND2012-7837
Unlimited Release
Printed September 2012

Scalable Assembly of Patterned Ordered Functional Micelle Arrays: Final LDRD Report

Hongyou Fan[a,b], Zaicheng Sun[b], Feng Bai[b], Anh Ta[b], Raid E. Haddad[b], Daniel M. Boye[c], Kevin A. Arpin[d], James H. Pikul[d], William P. King[d], and Paul V. Braun[d]

[a] Advanced Materials Lab, Sandia National Laboratories, P.O. 5800, Albuquerque, NM 87185-1349, USA
[b] Center for Micro-engineered Materials, Chemical and Nuclear Engineering Department, University of New Mexico, Albuquerque, NM 87131, USA
[c] Physics Department, Davidson College, Davidson, North Carolina 28035, USA
[d] Department of Materials Science and Engineering, University of Illinois, Urbana-Champaign, Urbana Illinois 61801, USA.

Abstract

In this project, we demonstrated the synthesis of polystyrene-polyvinylpyridyne (PS-PVP) micelles, functionalization of these micelles to form organic/inorganic composite nanoparticles, and template directed assembly of dynamic PS-PVP micelles into features defined via soft nanoimprint lithography. We demonstrated unique assembly properties of dynamic micellar nanoparticles by combining a top down lithographic nanopatterning technique with a solution-based bottom up self-assembly. The templates for the directed self-assembly of the micelles consisted of arrays of cylindrical recess features fabricated by nanoimprint lithography. Silica was coated on this patterned substrate and subsequently selectively functionalized with a positively charged molecular monolayer (*N*-(3-Trimethoxysilylpropyl) diethylenetriamine) to regulate the micelle-surface interactions. The self-assembled block co-polymer poly(styrene-b-4-vinyl pyridine), (PS_{480k} – PVP_{145k}) micelles were approximately 325nm in diameter in aqueous solutions (pH = 2.5) and 50nm in diameter in the dry state. The average number of micelles assembled per feature increased from less than 1 to 12 with increasing feature diameter in the range of 200nm – 1µm. Using a 2D model for maximum packing of circles in circular host features, the effective sphere size of the micelles during assembly was calculated to be 250nm in diameter. Thus, the micelles exhibited three characteristic sizes during assembly, 325nm in bulk solution, 250nm during assembly, and 50nm in the dry state. This dramatic variation in nanoparticle diameter during the assembly process offers unique opportunities for forming nanometer scale, multidimensional arrays not accessible using hard sphere building blocks.

This page intentionally left blank

Table of Contents

Abstract ……………………………………………………………………………..............3

Executive Summary..7

1. Introduction 9

2. Results and Discussion 10

3. Conclusions…………………………………………………………………………26

4. References 27

5. Distribution...28

List of Schemes and Figures

Scheme 1. Schematic description of self-assembly and formation of hydrophilic polymer nanoparticles. ……………………………………………….…………………….……….11

Scheme 2. Schematic illustration of the self-assembly and formation of monodispserse rare earth composite nanoparticles……………………………………………………………...13

Figure 1. TEM and SEM images of the monodisperse PS-PVP nanoparticles. 12

Figure 2. FTIR spectra of PS-PVP and PS-PVP/RE composite nanoparticles. 14

Figure 3. Monodisperse composite PS-PVP/lanthanide nanoparticles and size distribution......15

Figure 4. Optical properties of composite nanoparticles. ……………...………………………16

Figure 5. Fluorescent lifetime of PS-PVP/Eu nanoparticles in comparison with precursor $Eu(NO_3)_3 \cdot 5H_2O$. ……………………………………………………………...………...17

Figure 6. a) Schematic front and b) side view of functionalized templates during dip coating in an aqueous micelle solution (pH = 2.5). The micelles are shown both in solution and inside the recessed features of the functionalized template after removal from the solution…………………………………………………………………………………….19

Figure 7. a) Template directed assembly was not observed using non-functionalized patterned substrates coated with silica (no DEAS). Micelles non-specifically adhere to all surfaces. b) Representative template directed assembly of micelles using DEAS selectively functionalized patterned substrates. Micelles are found inside the recessed features of the patterned substrate but not on the top surface. Inset shows higher magnification image of micelle assembly inside a single feature with a 530nm diameter……………………………………………………..20

Figure 8. Average number of micelles per feature as a function of area per feature……...........21

Figure 9. The distribution of the number of micelles per feature for three different feature sizes a) 250nm b) 610nm and c) 1.04µm (all measured in diameter). …………….……………....22

Figure 10. 2D model for maximum packing of circular objects in circular features plotted as a step function (black line)…………………………………………………………………...23

Figure 11. Schematic of maximum packing assuming a micelle diameter of 250nm in the wet state during assembly……………………………………………………………………....24

Scalable Assembly of Patterned Ordered Functional Micelle Arrays: Final LDRD Report

Executive Summary

Control of 2&3D nanostructures with multifunction remains an unsolved challenge. Difficulties include scalable fabrication of rapid, reliable, inexpensive patterns with large areas and multifunction in various materials systems. The goal of this proposal is to combine ordered micelle assembly with both multidimensional patterning techniques for the first time, aiming to push "top-down/bottom-up" lithography into 2&3D structures and to better understand the fundamental mechanisms of nanoparticle assembly into higher dimensional structures. Together with NINE university partners from University of Illinois at Urbana-Champaign and University of New Mexico, we demonstrated the synthesis of polystyrene-polyvinylpyridyne (PS-PVP) micelles, functionalization of these micelles to form organic/inorganic composite nanoparticles, and template directed assembly of dynamic PS-PVP micelles into features defined via soft nanoimprint lithography. We demonstrated unique assembly properties of dynamic micellar nanoparticles by combining a top down lithographic nanopatterning technique with a solution-based bottom up self-assembly. The templates for the directed self-assembly of the micelles consisted of arrays of cylindrical recess features fabricated by nanoimprint lithography. Silica was coated on this patterned substrate and subsequently selectively functionalized with a positively charged molecular monolayer (*N*-(3-Trimethoxysilylpropyl) diethylenetriamine) to regulate the micelle-surface interactions. The self-assembled block co-polymer PS-PVP micelles were approximately 325nm in diameter in aqueous solutions (pH = 2.5) and 50nm in diameter in the dry state. The average number of micelles assembled per feature increased from less than 1 to 12 with increasing feature diameter in the range of 200nm – 1μm. Using a 2D model for

maximum packing of circles in circular host features, the effective sphere size of the micelles during assembly was calculated to be 250nm in diameter. Thus, the micelles exhibited three characteristic sizes during assembly, 325nm in bulk solution, 250nm during assembly, and 50nm in the dry state. This dramatic variation in nanoparticle diameter during the assembly process offers unique opportunities for forming nanometer scale, multidimensional arrays not accessible using hard sphere building blocks.

This project was funded through the Sandia National Institute of Nano-Engineering (NINE) Program. This project provided unique opportunities for graduate and undergraduate students to explore fundamental nanoscience and nano-engineering with focus on specific areas, such as nanoparticle synthesis, functionalization, and self-assembly as well as 2&3D patterning. The scope of this project reflects the urgent needs of NINE industry partners (Intel, ExxonMobil) to fabricate scalable patterned structures for IT and to develop facile and scalable self-assembly processes for fabrication of ordered arrays, and their use as masks/templates for metallic nanostructures in enhanced plasmonic, photonic, and sensor applications.

1. Introduction

Multidimensional patterning with precision, speed, and reproducibility at the nanometer scale is crucial for development in many fields including memory storage,[1-3] metamaterials,[4, 5] photonic crystals,[6] plasmonics,[7-9] solar energy harvesting,[10-12] energy storage,[13-15] and tissue engineering.[16, 17] Functional, multidimensional patterns at the nanometer scale will enable novel devices and properties that cannot be realized using unstructured materials. Conventional top-down photolithographic techniques are capable of producing features at the nanometer scale, however, are generally limited to planar geometries and select materials. Bottom-up self-assembly of materials offers unique opportunities to assemble matter in multiple dimensions at low-cost, however, understanding and optimizing self-assembly of functional structures remains an unsolved challenge and an active field of research.[18]

Organization of matter at the nanometer scale over large areas with low defect density can be accomplished by combining top-down lithographic nanopatterning with bottom-up self-assembly.[19] A number of research groups have followed this approach using micrometer or sub-micrometer sized rigid particles and patterned substrates.[20-26] One versatile approach pioneered by Xia[26] resulted in defect-free assembly of micrometer sized spherical particles over large areas. In that study, capillary forces directed spheres into lithographically defined features during de-wetting of an aqueous solution from a patterned surface. Capillary forces, however, decrease with decreasing particle size and competing effects including Brownian motion and electrostatic forces can play a significant role in assembly. Alivisatos, et. al. was able to control the assembly conditions, most notably, the template contact angle, to mitigate these competing factors and achieve accurate assembly of 50nm metallic and semiconducting nanoparticles into lithographically defined features.[27] In all these works, the physical dimensions of the assembled building blocks remained constant during the assembly process.

Herein, we investigate the potential for the template directed assembly of dynamic objects, namely self-assembled micelles. The micelles consist of a hydrophobic core (polystyrene) and a positively charged, hydrophilic shell (polyvinyl pyridine). The size of the micelles was closely related to the pH of the solution; at pH 2.5 the PVP chains are charged and thus repel each other, causing the shell to swell and the micelle diameter to reach 325nm. When dry, the micelles collapse to be 50nm in diameter. Dynamic building blocks such as these micelles offer unique opportunities for self-assembly, by allowing the formation of nanometer scale patterns and architectures that are not accessible using hard building blocks (e.g. non-close-packed structures). These micelles are also attractive as carriers of nanoparticles and other species that otherwise would not readily assembly in lithographically patterned substrates.[2, 28-30]

2. Results and Discussion

2.1. Formation of block copolymer micelles:

Scheme 1 illustrates the self-assembly process and preparation of the monodisperse nanoparticles. We used block copolymers polystyrene-*b*-polyvinylpyridine (PS-PVP) as the structure-directing agent. PS-PVP does not dissolve in water directly. Our strategy to form hydrophilic nanostructures is to dissolve PS-PVP in an organic solvent that dissolves both PS and PVP blocks to form a homogeneous solution. We then protonate PVP blocks to become water-soluble, which induces self-assembly of PS-PVP to form hydrophilic nanostructures. To start the preparation, PS-PVP was first dissolved in 1 ml DMF (or THF, dioxane), which is good solvent for both PS and PVP chains. A homogeneous and clear solution was obtained. 5 ml HCl aqueous solution ($pH < 4$) was then injected gradually with controlled injection speed using a syringe pump into the DMF solution under mild stirring. As the acidic aqueous solution was added, the PVP block was protonated and became soluble in aqueous phase. While gradually increase of amount of the aqueous acidic solution, the solvent environment becomes poor for the hydrophobic PS blocks, and PS blocks start to aggregate to form core of the nanoparticles surrounded by protonated hydrophilic PVP blocks. After complete injection of the HCl solution, particles solution was purified by centrifuging to remove the residual DMF. After several cycles of purification, the nanoparticles were collected and re-dispersed in DI water or alcohol.

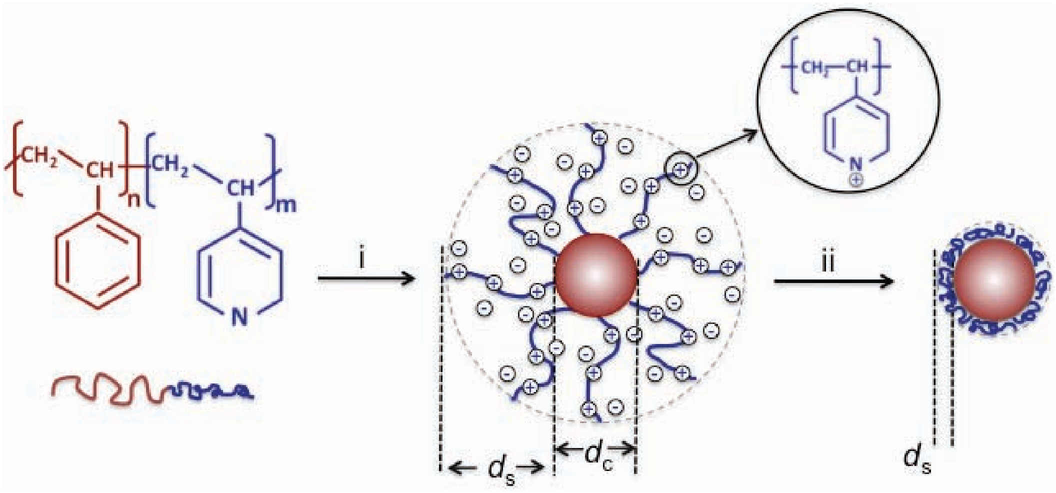

Scheme 1. Schematic description of self-assembly and formation of hydrophilic polymer nanoparticles. (i), acidic aqueous solution (HCl, pH < 4) is added into PS-PVP in DMF. (ii), after drying, nanoparticle size shrinks due to the collapse of PVP chains. d_s denotes the hydrodynamic radius of PVP shell and d_c the core diameter of PS.

During the injection course, the PS-PVP solution gradually turns to bluish color, which indicates formation of particles that scatter light. The final particles nanostructures were studied via electron microscopy (EM). **Figure 1** shows the EM images of the spherical nanoparticles. The nanoparticles have uniform size with narrow size distribution (standard deviation ~5%) and forming ordered arrays. The size of individual nanoparticles can be controlled from 20 nm up to ~50 nm depending on the size or molecular weight of both PS and PVP blocks. Using $PS_{35.5k}$-$PVP_{3.6k}$ (molecular weight of PS = 35.5K and of PVP = 3.6K), spherical nanoparticles with

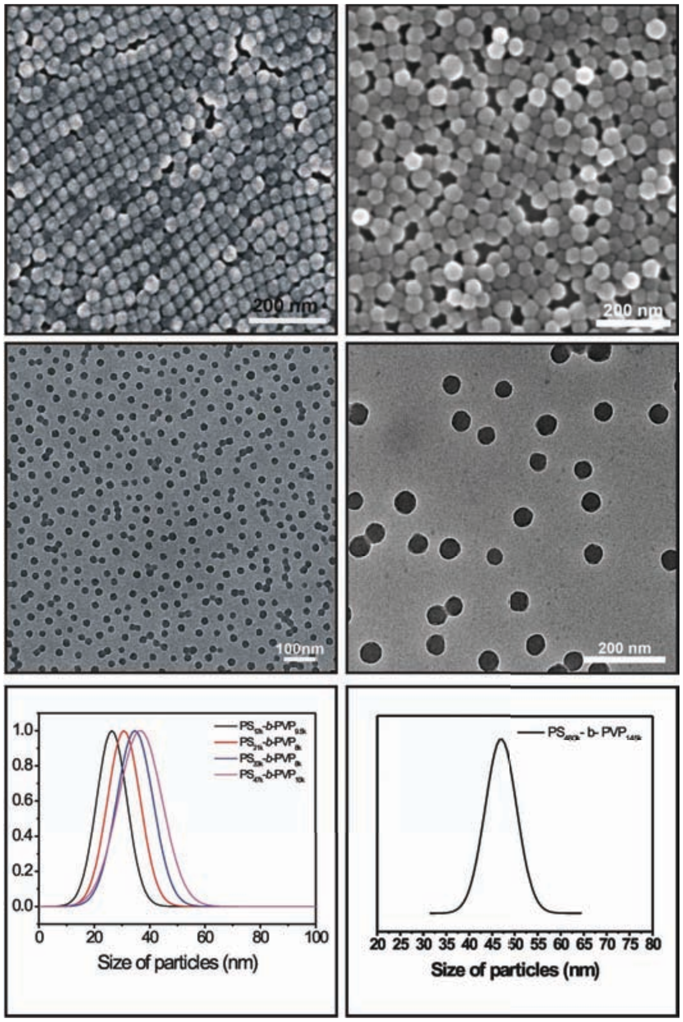

Figure 1. TEM and SEM images of the monodisperse PS-PVP nanoparticles.

diameter 25 ± 1.2 nm are obtained. By increasing molecular weight of PS and/or PVP, the nanoparticle size increases (**Figure 1**). As these measurements were formed on dried samples, the diameters include the size of PS core and the collapsed PVP chains. TEM images indicate that the particles possess uniform solid core without hollow cavities.

2.2. Functional organic/inorganic composite block copolymer micelles:

Scheme 2 describes the synthesis process of the organic/inorganic composite nanoparticles through preferential coordination between the PVP chains and lanthanide ions. In a typical preparation, the lanthanide rare earth precursor was first dissolved into 1,4-dioxane, forming a homogenous solution. The solution was then added into a 1,4-dioxane solution containing PS-PVP. Dioxane is a selective solvent for PS-PVP. PS block can dissolve in the dioxane very well, but PVP block only partly dissolve in it. The dioxane solution of PS-PVP is semitransparent and exhibits milky white color, which suggests aggregation PS-PVP and formation of PS-PVP micelles. After the $RE(NO_3)_3 \cdot nH_2O$ was added into the micelle solution, the RE ions were sequestered into the core of the micelles due to the interaction between RE ion and PVP blocks.

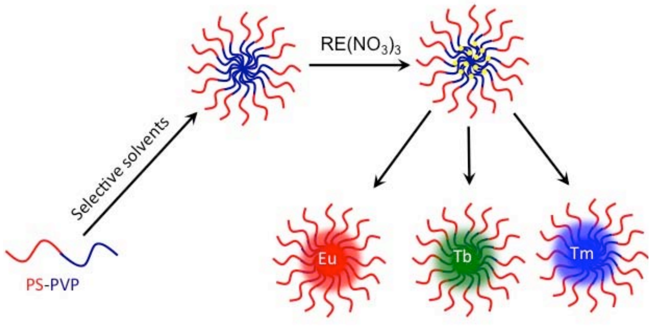

RE: Eu or Pr (red); Tb or Er (green); Tm or Ce (blue)

Scheme 2. Schematic illustration of the self-assembly and formation of monodispserse rare earth composite nanoparticles.

Insight into the coordination interaction between PVP and lanthanide ions was gained from Fourier transform infrared (FTIR) spectroscopy studies of the PS-PVP/lanthanide composite nanoparticles. **Figure 2** shows FTIR spectra of pure PS-PVP and PS-PVP/lanthanide composite nanoparticles. For pure PS-PVP polymer, the peaks at 1597, 1416, and 994 cm^{-1} are assigned to the characteristic vibrational modes of pyridine. In comparison with the spectra of pure PS-PVP, these PVP characteristic peaks have shifted to higher wave numbers for all lanthanide ions. PVP blocks show a rich basic Lewis character: the nitrogen atom incorporated within the aromatic ring tends to share a free electron pair with the available *f* electron orbits from lanthanide ions causing changes in the electron distributions of the pyridine ring. The result is a shift in energy for those peaks related to stretching modes of the pyridine ring. Such spectral shifts have also been observed in hydrogen bonding coordination behavior in other precursors and polymer systems[27-29]. In addition to FTIR studies, we have observed that key photoluminescence peak from PS-PVP/RE composites also blue shift due to the interactions between rare earth ions and block copolymers. Electron microscopy analysis further confirms the existence of rare earth elements within micellar nanoparticles (see **Figure 3**).

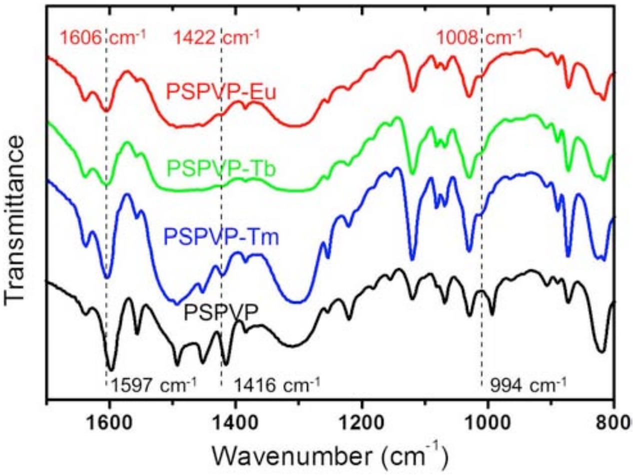

Figure 2. FTIR spectra of PS-PVP and PS-PVP/RE composite nanoparticles.

Typical transmission electron microscopy (TEM) images of as-made composite PS-PVP/lanthanide nanoparticles including PS-PVP/Tb, PS-PVP/Eu, and PS-PVP/Tm nanoparticles are illustrated in **Figure 3**. The images show that all nanoparticles are very monodisperse, demonstrating the high-quality production of composite nanoparticles. The average size of these composite nanoparticles is 25 nm in diameter with a standard size deviation of ~5%. TEM energy dispersion spectra (EDS) confirmed the existence of rare earth elements within the nanoparticles (**Figure 2**, A-C insets). TEM images further show that the nanoparticles form ordered hexagonal arrays. This is possibly due to the monodispersity and the van der Waals interaction of the PS shell of individual nanoparticles. **Figure 2D** shows the size distribution of the composite nanoparticles in solutions measured by using the dynamic light scattering (DLS) techniques.

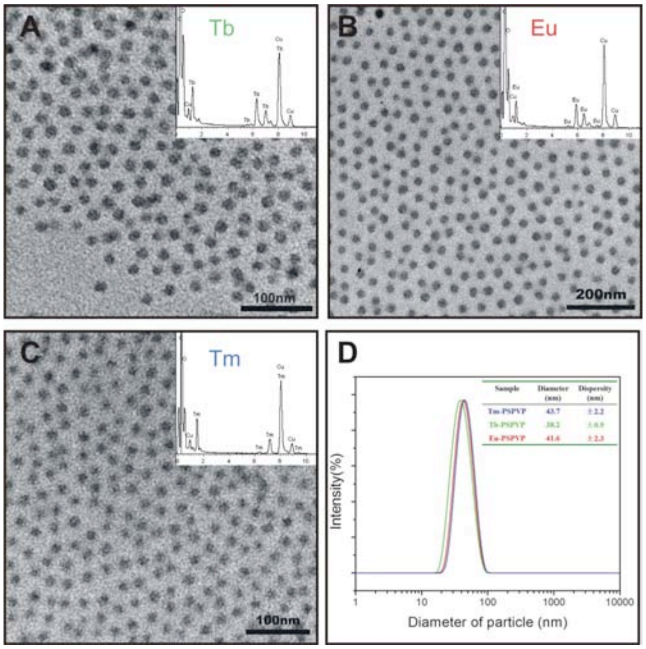

Figure 3. Monodisperse composite PS-PVP/lanthanide nanoparticles and size distribution. A-C, TEM image of the PS-PVP/Tb, PS-PVP/Eu, and PS-PVP/Tm nanoparticles, respectively; insets show the corresponding EDS. D, dynamic light scattering results of these nanoparticles.

DLS results further demonstrate the monodispersity and narrow size distribution of PS-PVP/RE nanoparticles. We observe a difference in size between the DLS and TEM results. In solutions, the nanoparticles show much larger size than those measured by TEM. This is likely caused by a drying effect. In the solution, the composite polymer nanoparticles are solvated and the polymer chains (especially PS block) are extended, therefore showing larger dynamic diameters. However, in the solid state (TEM sample), the nanoparticles are dried and shrunken, which results in a smaller size.

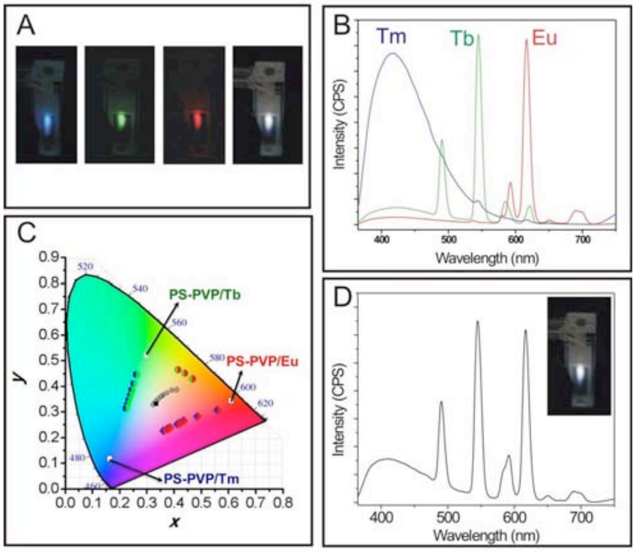

Figure 4. Optical properties of composite nanoparticles. A, optical pictures of nanoparticle solutions of PS-PVP/Tm (blue color), PS-PVP/Tb (green color), PS-PVP/Eu (red color), and the mixture of above three solutions (white color, with volume ratio of each solution: PS-PVP/Tm:PS-PVP/Tb:PS-PVP/Eu = 8:1:1) excited with a 300 nm UV light. B, PL spectra of nanoparticle solutions of PS-PVP/Tm, PS-PVP/Tb, and PS-PVP/Eu. C, Luminescence spectra of polymer nanoparticle solutions plotted on CIE diagram and compositions trajectory to tune color through stoichiometric mixing. D, PL spectra of the white color solution in B.

Figure 4A shows the photoluminescent (PL) spectra of PS-PVP/Tm (414 nm, blue), PS-PVP/Tb (545 nm, green), and PS-PVP/Eu (617 nm, red) nanoparticles. The PL spectra confirm that the composite nanoparticles retain the optical properties of the corresponding lanthanide ions. Figure 4A shows photographs of three PS-PVP/RE solutions excited by 300 nm UV light.

It shows, respectively, the three primary color of blue, green, red and white light emitted from PS-PVP/Tm, PS-PVP/Tb, PS-PVP/Eu, and a mixture of above three solutions with a volume ratio of 8:1:1. The mixture emits white light with the CIE coordinates x=0.33 and y=0.34. The coordination interaction between the PVP chains and lanthanide ions essentially sequesters the lanthanide ions completely within polymer nanoparticles, leaving PS as the outer shell of the nanoparticles. Thus, the composite PS-PVP/RE nanoparticles can independently emit the corresponding color of the ions that are encapsulated within the nanoparticles. In addition to the three primary colors (red, green, and blue), variations of color can be tuned through the mixture of nanoparticles of independent color. Therefore, a large area of the color map can be accessed by simply mixing 2 or 3 primary polymer nanoparticles solutions and following the trajectory of CIE coordinates through compositional changes of the nanoparticles. Using such a procedure, we have fabricated solutions with a variety of emission colors using these composite nanoparticles.

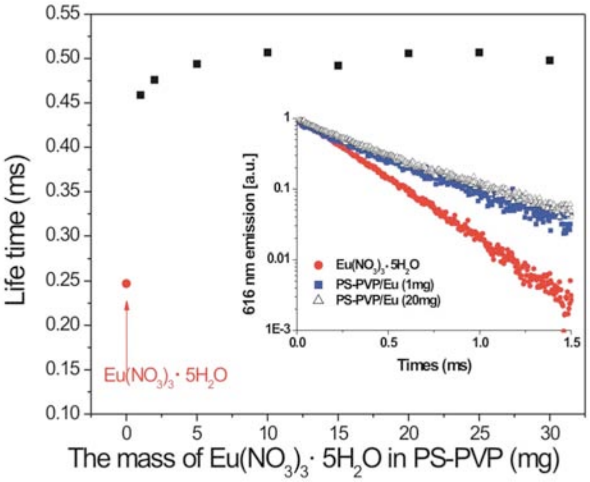

Figure 5. Fluorescent lifetime of PS-PVP/Eu nanoparticles in comparison with precursor $Eu(NO_3)_3 \cdot 5H_2O$.

We have measured the fluorescent lifetime of the composite nanoparticle (PS-PVP/Eu) in comparison with $Eu(NO_3)_3 \cdot 5H_2O$. The luminescence decays for both PS-PVP/Eu and $Eu(NO_3)_3 \cdot 5H_2O$ can be fit by single exponentials as $I=I_0 \exp(-t/t)$, where t is the 1/*e* lifetime of rare earth ions. This indicates that all of the Eu^{3+} ions have similar environments within the composite nanoparticles. The lifetime of excited state for Eu^{3+} can be determined by the fits shown in the **Figure 5**. It is shown that the luminescence lifetime of PS-PVP/Eu (~0.5 ms) is longer than those of Eu^{3+} in the dioxane solution (~0.25 ms). A likely cause is that water molecules complexed with Eu^{3+} have been replaced by pyridine molecules in the PS-PVP. Water molecules promote non-radiative relaxation of excited Eu^{3+}. Non-radiation relaxation is depressed by the replacement of pyridine.

2.3. Patterning block copolymer micelles:

2.3.1 Micelle Packing in Patterned Substrates

Patterned substrates for the directed self-assembly of our dynamic micellar building blocks were fabricated using a soft nanoimprint lithography technique,[31, 32] useful for manufacturing large area, defect free, recessed features with varying dimensions and shapes. A simple dip coating procedure was used to drive template directed self-assembly of micelle arrays (**Figure 6**). Capillary forces alone during de-wetting (as the drying line passes down the substrate) are insufficient on their own to direct assembly of the dynamic micelles into the template features. After dip coating nearly neutral substrates (un-functionalized silica in a pH = 2.5), directed micelle assembly was not observed; micelles non-specifically deposited within the recessed features and on the top surface of the template (**Figure 7a**). It is known that electrostatics can significantly influence template directed assembly.[35] This effect is of course strongest when the particles are highly charged, as is the case for this study. Using this effect to our advantage, we spatially modified the electrostatic environment of the template to assist with the directed assembly of micelles. A soft lithography approach was utilized to selectively functionalize the top surface of the template with a positively charged monolayer, leaving the bottom of the features relatively uncharged. After printing, only the top surface of the templates experienced a charge inversion, going from slightly negative (silica at pH 2.5) to positive.

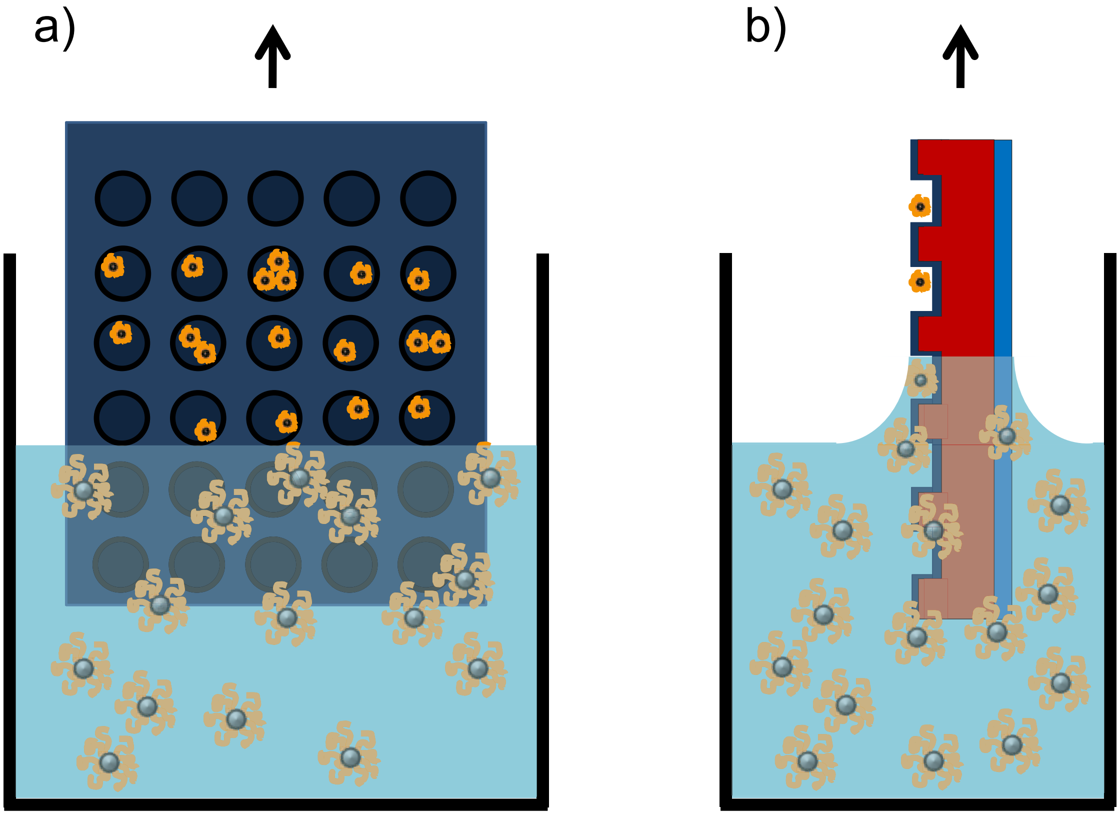

Figure 6. a) Schematic front and b) side view of functionalized templates during dip coating in an aqueous micelle solution (pH = 2.5). The micelles are shown both in solution and inside the recessed features of the functionalized template after removal from the solution.

This charge inversion process was vital to achieving template directed assembly of dynamic micelle arrays. Figure 3b presents an image of representative micelle assembly observed after dip coating onto substrates selectively functionalized with DEAS; micelles are directed into the recessed features during assembly with no micelles remaining on the top surface.

Previous studies have shown that the number of building blocks that can be assembled into a template feature is determined by the ratio between the dimensions of the template feature and the dimensions of the building block.[26] This relationship was studied by assembling micelles

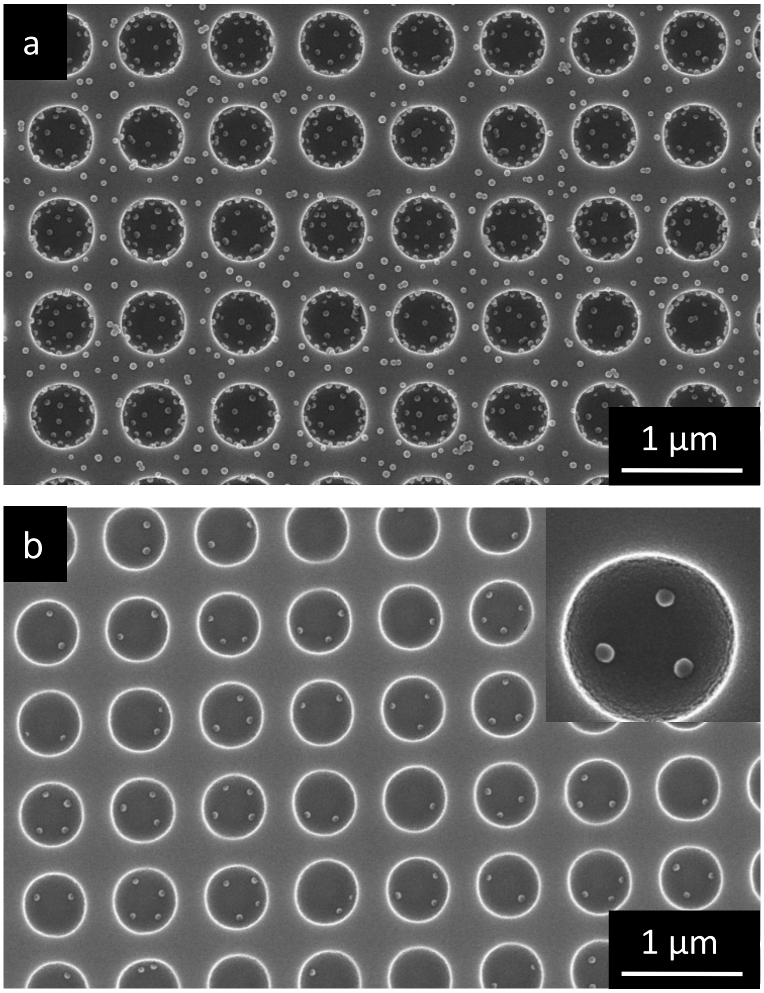

Figure 7. a) Template directed assembly was not observed using non-functionalized patterned substrates coated with silica (no DEAS). Micelles non-specifically adhere to all surfaces. b) Representative template directed assembly of micelles using DEAS selectively functionalized patterned substrates. Micelles are found inside the recessed features of the patterned substrate but not on the top surface. Inset shows higher magnification image of micelle assembly inside a single feature with a 530nm diameter.

into various templates, each with a different characteristic feature dimension. The diameter of the feature, as measured at the top surface of the patterned substrates, was used as the characteristic feature dimension ($D_{Template}$). Not surprisingly, the average number of micelles per feature (N_{AVG}) increased as $D_{Template}$ increased from 200nm to 1µm. The average number of micelles per feature was calculated by manually counting the number of micelles observed in at least 50 features.

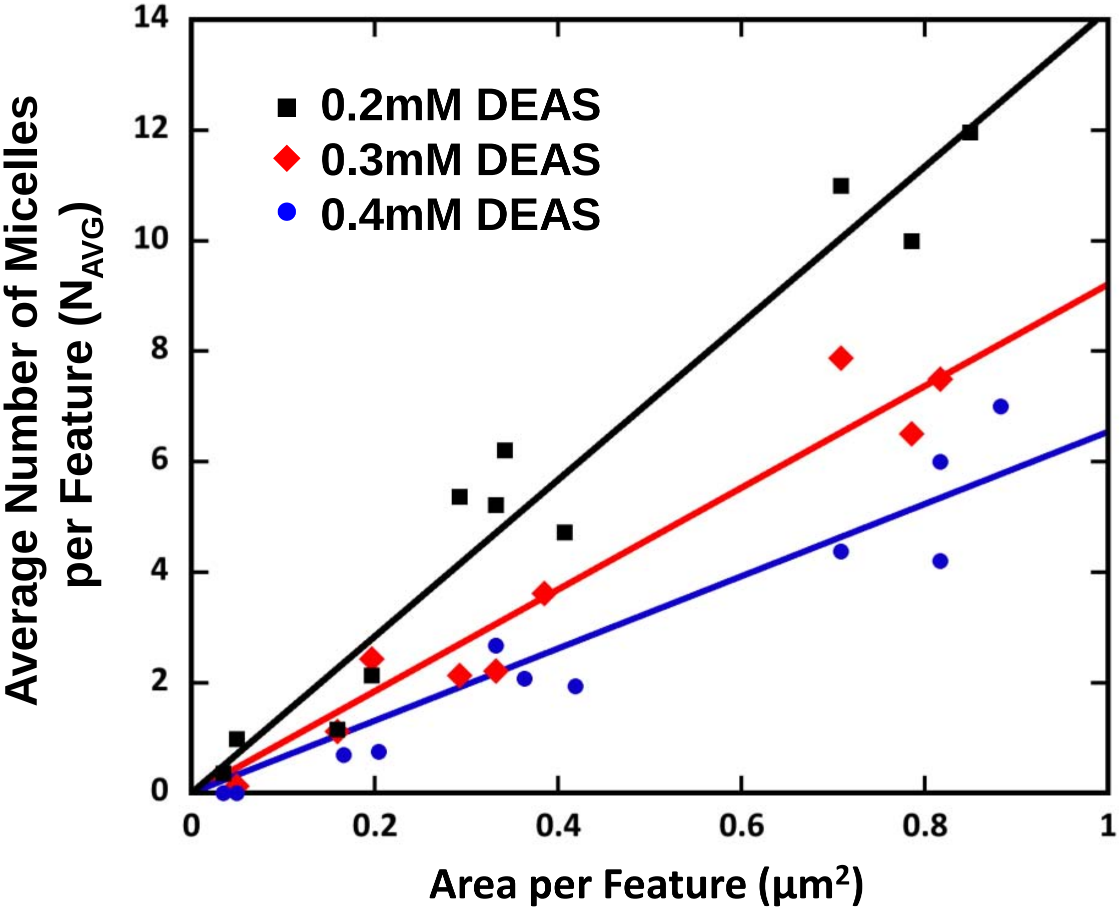

Figure 8. Average number of micelles per feature as a function of area per feature. Three data sets are included representing N_{AVG} resulting from assembly using templates functionalized with different DEAS concentrations in hexane (0.2, 0.3, and 0.4mM). Maximum packing was observed for 0.2mM DEAS. Lower concentrations of DEAS resulted in non-specific attachment of micelles on the top surface of the patterned substrate. Increased concentrations of DEAS resulted in fewer micelles per feature over all feature sizes because of DEAS molecules diffusing to the bottom of the recessed features through the vapor phase. Linear regressions are included to emphasize the difference in N_{AVG} as a function of feature size for the three different concentrations of DEAS used for printing.

The counted averages were plotted as a function of the area per template feature (calculated using $D_{Template}$) and displayed in **Figure 8**. The relationship between N_{AVG} and feature size was reproducible over large areas of each substrate and multiple samples. Representative distributions of count data for three different feature sizes (0.25μm,

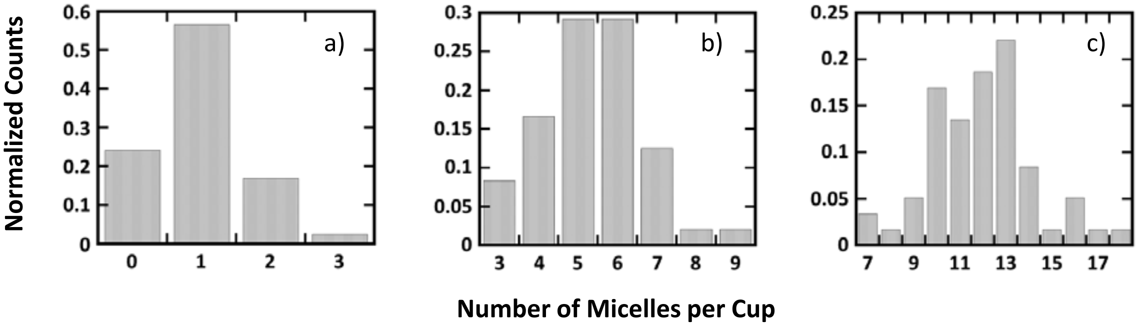

Figure 9. The distribution of the number of micelles per feature for three different feature sizes a) 250nm b) 610nm and c) 1.04μm (all measured in diameter). These are representative of the data over large areas of the sample. All three distributions represent data counted from sample printed with 0.2mM DEAS.

0.61μm, and 1.04μm) are presented in **Figure 9a**, **b**, and **c**, respectively. The distributions of the count data were close to normal around the calculated averages demonstrating that the data is generally not clustered and is uniformly distributed over large areas.

Due to the dynamic nature of the micelles, the characteristic size of our building blocks during template directed assembly was significantly different from the characteristic size of the micelles either in bulk solution or the dry state. We considered assembly after printing with 0.2mM DEAS in hexane to be the case of maximum packing. The effect of DEAS concentration on micelle assembly is presented in **Figure 8** and will be explained, in detail, in the next section. To summarize, lower concentrations of DEAS resulted in non-specific attachment of micelles on the top surface of the patterned substrates. However, at higher concentrations of DEAS, we suspect some DEAS is deposited in the bottom of the features, altering the micelle-surface interaction, and decreasing the observed N_{AVG}. The assembly data acquired for this concentration of

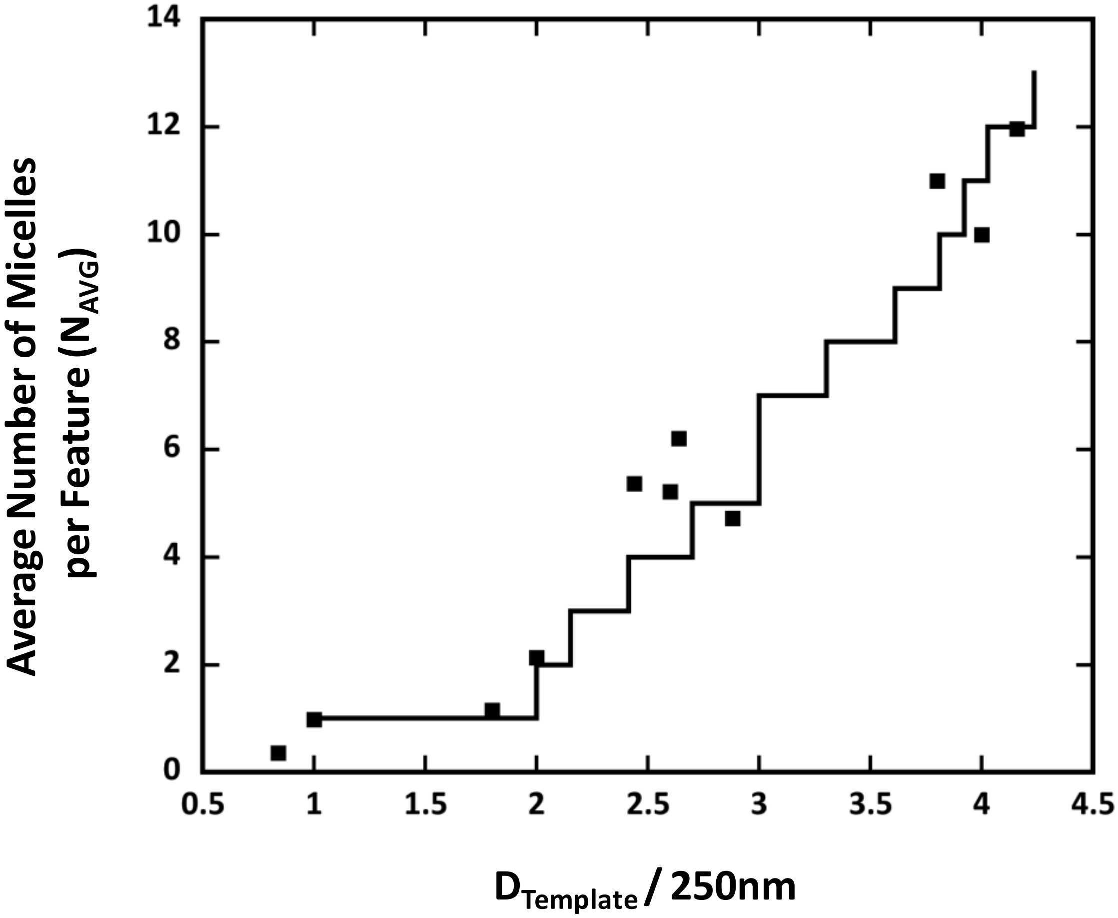

Figure 10. 2D model for maximum packing of circular objects in circular features plotted as a step function (black line).[36] The average number of micelles per feature is plotted as a function of the ratio between the diameter of the host feature and the diameter of the micelles (black dots). Assuming a micelle diameter of 250nm, the counted data for N_{AVG} as a function of feature size matches closely to the calculated maximum packing density.

DEAS (0.2mM) was compared to a 2D model for the maximum packing expected for circles in circular features.[36] Since the depth of the cylindrical features (~250nm) is less than the diameter of the micelles in bulk solution (325nm), and the micelles are repulsive, we expect monolayer packing and thus we can use this 2D model to understand the micelle assembly. Using this 2D model, the ratio between the diameter of a host circle and the diameter of circles being packed was plotted in **Figure 10** as a step function. The average number of micelles per feature as a function of the same ratio between the diameter of the template feature and the diameter of the micelle matches well to the expected trend (**Figure 10**). The measured data matches the calculated step function best for a micelle diameter of 250nm. Thus, the characteristic diameter of the micelles during assembly appears to be 75nm less than the diameter in bulk solution. **Figure 11** schematically shows this maximum packing of micelles when in the swollen state with a diameter of 250nm. We propose that de-swelling of the PVP shell or overlap of shells on adjacent micelles during assembly could explain the difference in micelle diameter in bulk solution and micelle diameter during template directed assembly.

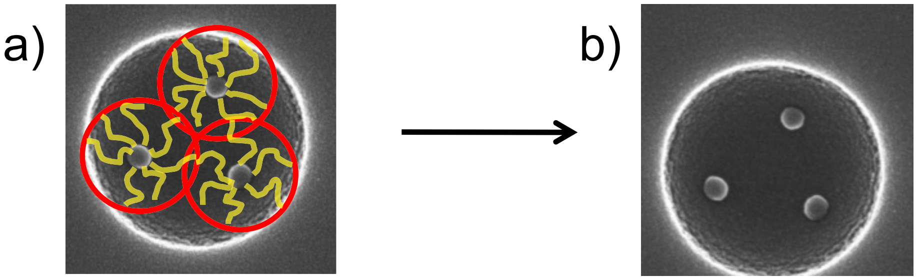

Figure 11. a) Schematic of maximum packing assuming a micelle diameter of 250nm in the wet state during assembly. b) After drying, the micelles remain in their directed positions, but condense to a diameter of 50nm. The feature diameter is 530nm.

The dramatic shrinking of the micelles while remaining in a defined location, (**Figure 11**) and note that the particle are almost never touch in the dry state, (**Figure 7b**) offers unique opportunities for the self-assembly of functional, multidimensional, nanometer scale arrays. Moreover, these dynamic structures represent a bridge between the larger scale of top down lithographic methods and the fine nanometer scale achievable using bottom up self-assembly. The manufacturing of nanometer scale architectures will not be possible using one of these techniques alone, however, it will be the combination of these two techniques that will be at the forefront of research involving the fabrication of functional devices with nanometer scale features. Self-assembly using dynamic building blocks presents one potential integration method.[37-39]

2.3.2 DEAS Monolayer Printing and Micelle Assembly

Slight alterations in the DEAS printing protocol significantly altered the observed N_{AVG} for a given template feature size. More specifically, the concentration of DEAS in hexane and printing time altered N_{AVG} observed after assembly for a given feature size. We quantified this effect by studying assembly using three different concentrations of DEAS in hexane for printing while keeping the printing time constant (30 seconds). The resultant N_{AVG} as a function of feature size for the three DEAS concentrations are presented in **Figure 8**. Increasing the concentration of DEAS resulted in fewer average numbers of micelles per feature (lower N_{AVG}, for all feature sizes).

We hypothesize that this difference in assembly could be attributed to DEAS depositing inside the recessed features during assembly through the vapor phase. DEAS printed inside cups could alter the interaction energy of the micelles with the silica surface. Micelles remain inside the recessed features during drying because the electrostatic interaction energy between the slight negative charge of the bottom of the recessed feature and the positive charge of the micelles is greater than the capillary force trying to keep the micelles in solution during de-wetting (drying). If this electrostatic interaction energy is decreased, potentially by the deposition of positively charged DEAS molecules, the capillary force may dominate, pulling micelles out of recessed features during de-wetting.

To support this hypothesis, a lower molecular weight (higher vapor pressure) amino silane, 3-aminopropytriethocysilane (APS), was printed on the top surface of nanoimprint templates instead of DEAS, using the same printing procedure. After dip coating, the APS functionalized templates showed almost no micelles remaining on the template (inside the recessed features or on the top surface) for all three concentrations (0.2mM, 0.3mM, 0.4mM). The APS experiment suggests that the silane volatility alters the resultant electrostatic environment of the bottom of the recessed features. While DEAS is less volatile than APS, we expect that some DEAS is diffusing through the vapor phase into the recessed features, most prominently at higher DEAS concentrations. Thus, vapor phase transport most likely contributes to the observation that increasing the concentration of DEAS resulted in few micelles per feature.

3. Conclusion

Here we demonstrated the synthesis of PS-PVP micelles, functionalization of these micelles to form organic/inorganic nanoparticles, and template directed assembly of dynamic PS-PVP core-shell micelles into features defined via soft nanoimprint lithography. Capillary forces alone were insufficient to direct micelles into the template features. A positively charged molecular monolayer was selectively printed on the top surface of the patterned template providing a surface with coupled topographic and electrostatic features. This monolayer was essential to achieving successful micelle assembly over large areas. The dynamic micelles had 3 characteristic diameters observed at different stages of the assembly process: 325nm in bulk solution, 250nm during assembly, and 50nm in the dry state. This work here is the first example of assembly of dynamic objects into topographic features, and we expect that these three dramatically different dimensions could be exploited for applications in nanometer scale assembly that cannot be achieved using hard sphere particles.

4. References

1. C. Chappert, A. Fert and F. N. Van Dau, *Nature Materials*, 2007, **6**, 813-823.
2. B. N. Mbenkum, A. Diaz-Ortiz, L. Gu, P. A. van Aken and G. Schutz, *Journal of the American Chemical Society*, 2010, **132**, 10671-10673.
3. A. Ethirajan, U. Wiedwald, H. G. Boyen, B. Kern, L. Y. Han, A. Klimmer, F. Weigl, G. Kastle, P. Ziemann, K. Fauth, J. Cai, R. J. Behm, A. Romanyuk, P. Oelhafen, P. Walther, J. Biskupek and U. Kaiser, *Advanced Materials*, 2007, **19**, 406-+.
4. N. Liu, H. C. Guo, L. W. Fu, S. Kaiser, H. Schweizer and H. Giessen, *Nature Materials*, 2008, **7**, 31-37.
5. J. K. Gansel, M. Thiel, M. S. Rill, M. Decker, K. Bade, V. Saile, G. von Freymann, S. Linden and M. Wegener, *Science*, 2009, **325**, 1513-1515.
6. K. A. Arpin, A. Mihi, H. T. Johnson, A. J. Baca, J. A. Rogers, J. A. Lewis and P. V. Braun, *Advanced Materials*, 2010, **22**, 1084-1101.
7. D. K. Gramotnev and S. I. Bozhevolnyi, *Nature Photonics*, 2010, **4**, 83-91.
8. W. L. Barnes, A. Dereux and T. W. Ebbesen, *Nature*, 2003, **424**, 824-830.
9. C. Rockstuhl, C. Menzel, T. Paul and F. Lederer, *Physical Review B*, 2009, **79**, -.
10. H. A. Atwater and A. Polman, *Nature Materials*, 2010, **9**, 205-213.
11. A. Mihi and H. Miguez, *Journal of Physical Chemistry B*, 2005, **109**, 15968-15976.
12. P. Bermel, C. Luo, L. Zeng, L. C. Kimerling and J. D. Joannopoulos, *Optics Express*, 2007, **15**, 16986-17000.
13. J. W. Long, C. P. Rhodes, M. S. Doescher, M. S. Logan and D. R. Rolison, *Abstracts of Papers of the American Chemical Society*, 2003, **225**, U973-U973.
14. D. R. Rolison and H. S. White, *Langmuir*, 1999, **15**, 649-649.
15. P. Banerjee, I. Perez, L. Henn-Lecordier, S. B. Lee and G. W. Rubloff, *Nature Nanotechnology*, 2009, **4**, 292-296.
16. R. A. Barry, R. F. Shepherd, J. N. Hanson, R. G. Nuzzo, P. Wiltzius and J. A. Lewis, *Advanced Materials*, 2009, **21**, 2407-+.
17. J. H. Huang, S. V. Grater, F. Corbellinl, S. Rinck, E. Bock, R. Kemkemer, H. Kessler, J. D. Ding and J. P. Spatz, *Nano Letters*, 2009, **9**, 1111-1116.
18. M. P. Stoykovich, H. Kang, K. C. Daoulas, G. Liu, C. C. Liu, J. J. de Pablo, M. Mueller and P. F. Nealey, *Acs Nano*, 2007, **1**, 168-175.
19. J. A. Rogers, H. H. Lee, *Unconventional Nanopatterning Techniques and Applications*, John Wiley & Sons, Inc., 2009.
20. J. Hur and Y. Y. Won, *Soft Matter*, 2008, **4**, 1261-1269.
21. N. N. Khanh and K. B. Yoon, *Journal of the American Chemical Society*, 2009, **131**, 14228-+.
22. A. vanBlaaderen, R. Ruel and P. Wiltzius, *Nature*, 1997, **385**, 321-324.
23. C. Kuemin, K. C. Huckstadt, E. Lortscher, A. Rey, A. Decker, N. D. Spencer and H. Wolf, *Advanced Materials*, 2010, **22**, 2804-+.
24. R. J. Jackman, D. C. Duffy, E. Ostuni, N. D. Willmore and G. M. Whitesides, *Analytical Chemistry*, 1998, **70**, 2280-2287.
25. H. K. Choi, S. H. Im and O. O. Park, *Langmuir*, 2010, **26**, 12500-12504.
26. M. Rycenga, P. H. C. Camargo and Y. N. Xia, *Soft Matter*, 2009, **5**, 1129-1136.
27. Y. Cui, M. T. Bjork, J. A. Liddle, C. Sonnichsen, B. Boussert and A. P. Alivisatos, *Nano Letters*, 2004, **4**, 1093-1098.

28. B. S. Kim, J. M. Qiu, J. P. Wang and T. A. Taton, *Nano Letters*, 2005, **5**, 1987-1991.
29. Z. B. Ge, Y. J. Kang, T. A. Taton, P. V. Braun and D. G. Cahill, *Nano Letters*, 2005, **5**, 531-535.
30. B. L. Sanchez-Gaytan, W. H. Cui, Y. J. Kim, M. A. Mendez-Polanco, T. V. Duncan, M. Fryd, B. B. Wayland and S. J. Park, *Angewandte Chemie-International Edition*, 2007, **46**, 9235-9238.
31. S. Jeon, J. U. Park, R. Cirelli, S. Yang, C. E. Heitzman, P. V. Braun, P. J. A. Kenis and J. A. Rogers, *Proceedings of the National Academy of Sciences of the United States of America*, 2004, **101**, 12428-12433.
32. J. M. Yao, A. P. Le, S. K. Gray, J. S. Moore, J. A. Rogers and R. G. Nuzzo, *Advanced Materials*, 2010, **22**, 1102-1110.
33. E. Asenath-Smith and W. Chen, *Langmuir*, 2008, **24**, 12405-12409.
34. J. A. Howarter and J. P. Youngblood, *Langmuir*, 2006, **22**, 11142-11147.
35. J. Aizenberg, P. V. Braun and P. Wiltzius, *Physical Review Letters*, 2000, **84**, 2997-3000.
36. S. Kravitz, *Mathematics Magazine*, 1967, **40**, 65-71.
37. G. M. Whitesides, J. K. Kriebel, B. T. Mayers, in *Nanoscale Assembly: Chemical Techniques* ed. W. T. S. Huck, Springer, 2005.
38. D. Qin, Y. N. Xia, B. Xu, H. Yang, C. Zhu and G. M. Whitesides, *Advanced Materials*, 1999, **11**, 1433-1437.
39. B. A. Parviz, D. Ryan and G. M. Whitesides, *Ieee Transactions on Advanced Packaging*, 2003, **26**, 233-241.

5. Distribution

1	MS 1349	Hongyou Fan, 1815
1	MS 1349	William Hammetter, 1815
1	MS 0359	Donna Chavez, 1911
1	MS 0899	Technical Library, 9536 (electronic copy)

Sandia National Laboratories